Check for updates

Two-dimensional Janus Si$_2$OX (X = S, Se, Te) monolayers as auxetic semiconductors: theoretical prediction

Nguyen P. Q. Anh,[a] N. A. Poklonski, [b] Vo T. T. Vi, [c] Cuong Q. Nguyen [de] and Nguyen N. Hieu [*de]

The auxetic materials have exotic mechanical properties compared to conventional materials, such as higher indentation resistance, more superior sound absorption performance. Although the auxetic behavior has also been observed in two-dimensional (2D) nanomaterials, to date there has not been much research on auxetic materials in the vertical asymmetric Janus 2D layered structures. In this paper, we explore the mechanical, electronic, and transport characteristics of Janus Si$_2$OX (X = S, Se, Te) monolayers by first-principle calculations. Except for the Si$_2$OTe monolayer, both Si$_2$OS and Si$_2$OSe are found to be stable. Most importantly, both Si$_2$OS and Si$_2$OSe monolayers are predicted to be auxetic semiconductors with a large negative Poisson's ratio. The auxetic behavior is clearly observed in the Janus Si$_2$OS monolayer with an extremely large negative Poisson's ratio of -0.234 in the x axis. At the equilibrium state, both Si$_2$OS and Si$_2$OSe materials exhibit indirect semiconducting characteristics and their band gaps can be easily altered by the mechanical strain. More interestingly, the indirect–direct bandgap phase transitions are observed in both Si$_2$OS and Si$_2$OSe monolayers when the biaxial strains are introduced. Further, the studied Janus structures also exhibit remarkably high electron mobility, particularly along the x direction. Our findings demonstrate that Si$_2$OS and Si$_2$OSe monolayers are new auxetic materials with asymmetric structures and show their great promise in electronic and nanomechanical applications.

1 Introduction

The auxetic material is a material possessing a negative Poisson's ratio (NPR). The material contracts laterally when compressed and expands laterally when stretched. NPR has been observed in both bulk and low-dimensional materials. For example, perovskite,[1] honeycombs,[2] ceramics,[3] and cubic metals[4] are bulk materials possessing the NPR phenomena. NPR has been also found in one-dimensional (1D) structures.[5,6] Particularly, both normal and auxetic behaviors coexist in 1D poly[5]asterane.[7] Recently, the auxetic effects have also been revealed in two-dimensional (2D) structures. Black phosphorus is the first 2D material reported to have an NPR with a small value of -0.027.[8] Later, the auxetic behavior has also been found in other 2D layered nanomaterials such as borophene,[9]

Be$_5$C$_2$,[10] h-BN,[11] and 1T phase of transition metal dichalcogenides.[12] In parallel with the bulk and 2D materials, the auxetic effect is also explored in van der Waals superlattices.[13] The graphene/hexagonal-BN superlattice has an NPR with values of -0.109 and -0.111 depending on its atomic stacking configuration.[13] The origin of auxetic phenomena is found to be the structure of the material. It can be explained by the wrinkled or re-entrant crystal structure. The auxetic materials have exotic mechanical properties compared to conventional materials, such as higher indentation resistance,[14] more superior sound absorption performance.[15] Therefore, NPR materials have application prospects in the fields of industry,[16] biomedicine,[17] and sensors.[18]

Up to now, the variety and application prospects of 2D materials have been extensively demonstrated.[19–21] Among them, the SiS monolayer is a typical compound for 2D structures with extraordinary physical characteristics. Particularly, 2D SiS layers can be stable in different polymorphs, including *Pma*2-SiS, *Pmma*-SiS, and silicene sulfide.[22] The SiS monolayer was found to exhibit mechanical, energetic, and thermal stability.[23] Besides, the SiS monolayer possesses excellent mechanical and electronic properties. The SiS exhibits semiconducting features with a tunable direct energy gap and directionally anisotropic carrier mobility. The mobility of

[a] *Faculty of Electrical, Electronics and Materials Technology, University of Sciences, Hue University, Hue, 530000, Viet Nam*

[b] *Faculty of Physics, Belarusian State University, Minsk 220006, Belarus*

[c] *Faculty of Basic Sciences, University of Medicine and Pharmacy, Hue University, Hue 530000, Viet Nam*

[d] *Institute of Research and Development, Duy Tan University, Da Nang 550000, Viet Nam. E-mail: hieunn@duytan.edu.vn*

[e] *Faculty of Natural Sciences, Duy Tan University, Da Nang 550000, Viet Nam*

electrons in the SiS structure is superior with a value of 1.11×10^4 cm^2 V^{-1} s^{-1}. Most importantly, SiS exhibits high NPR with a value of -0.19 in the x axis.[23] Therefore, the SiS monolayer has great promise in applications for nanomechanics and optoelectronics.[23]

Since the experimental synthesis of 2D vertically asymmetric MoSSe sheet,[24,25] 2D Janus structures have become an important object in the studies in the material science field.[26–29] The 2D Janus monolayers exhibit many exotic physical properties compared to their original symmetric counterparts.[30–34] Recently, a few works have presented a particularly intriguing property of the Janus structures, namely the auxetic behavior. The Poisson's ratio with a negative value has been found in both in-plane directions. For example, the Si$_2$SSe monolayer has NPR with a value of -0.11 (-0.08) along the x (y) axis.[23] In term of Si$_2$XY (X/Y = S, Se, Te) structures, NPR values lie between -0.062 and -0.113 (-0.082 and -0.122) along the x (y) axis.[35] However, little research on the NPR effect has been performed on asymmetric Janus structures. Therefore, the search for Janus structures with auxetic behavior is very important. Motivated by these problems, we report the mechanical features, electronic characteristics, and carrier mobility of Janus 2D Si$_2$OX (X = S, Se, Te) monolayers using density functional theory (DFT) method. It is demonstrated that the Si$_2$OX monolayers, except for Si$_2$OTe, are semiconductors with stable structures, high carrier mobility, and strain-controlled band gap. Most importantly, the NPR phenomena are explored in the Janus Si$_2$OX monolayers. With these findings, we hope to provide fundamental insights and promote extensive studies for Janus structures as well as auxetic materials.

2 Theoretical model and computational details

Our first-principles simulations were carried out based on DFT technique by using the Vienna *ab initio* simulation package.[36,37] We used the projector augmented wave (PAW) method to investigate the core-electron interactions.[36] Generalized gradient approximation (GGA) parameterized by Perdew, Burke, and Ernzerhof (PBE)[38] was performed for the crystal structure optimizations. Dipole correction is included to treat the errors induced by the periodic boundary condition.[39] The Brillouin zone of the studied structures was sampled with a $15 \times 15 \times 1$ k-mesh by Monkhorst–Pack technique.[40] The GGA-PBE functional was used for the optimization of the crystal structures. The crystal structures were totally relaxed until the Hellman–Feynman force was less than 1×10^{-3} eV Å^{-1} and the total energy was converged to 10^{-8} eV. An energy cut-off of 500 eV was selected for the plane-wave basis functions. The GGA-PBE method was used to describe the electron exchange–correlation interaction. Also, the hybrid functional by Heyd–Scuseria–Ernzerhof (HSE06) was used to correct the band gap errors of the considered structures.[41] The van der Waals corrections were treated by using the DFT-D3 method suggested by Grimme.[42] To avoid the periodic interactions in the vertical direction, we inserted a vacuum distance of 20 Å along the z axis. The phonon

spectra of the studied materials were calculated by using the PHONOPY code[43] based on the finite displacement technique. The *ab initio* molecular dynamics (AIMD) simulations with the NVT ensemble (the number of particles N, the calculated cell volume V, and temperature T were fixed) were used to investigate the thermodynamic stabilities of the considered materials.[44] The deformation potential (DP) method was adopted to compute the carrier mobilities.[45]

3 Results and discussion

3.1 Crystal structure, stability, and mechanical characteristics

The crystal structures of the vertical asymmetric Janus Si$_2$OX (X = S, Se, and Te) monolayer are shown in Fig. 1. The Janus Si$_2$OX monolayers belong to *Pma*2 symmetry. We can construct the Janus Si$_2$OX from the *Pma*2-SiX monolayer[22] by substituting the bottom chalcogen layer X with the oxygen layer as presented in Fig. 1. We can see that the unit cell of the Si$_2$OX monolayers contains 8 atoms, including four Si, two O, and two X atoms, as shown in Fig. 1(a). It is found that Janus Si$_2$OX monolayers possess an anisotropic crystal structure. The lattice constants $a(b)$ of Si$_2$OS, Si$_2$OSe, and Si$_2$OTe are calculated to be 5.92(3.90), 5.92(3.92), and 5.97(4.03) Å, respectively. It is shown that there is no significant different in bond angle $\varphi_{\angle \text{Si}^-\text{O}^-\text{Si}}$ between the structures. Meanwhile, the large different in $\varphi_{\angle \text{Si–X–Si}}$ between the structures is found. The obtained $\varphi_{\angle \text{Si–X–Si}}$ is found to be 87.82°, 80.37°, and 72.23° for Si$_2$OS, Si$_2$OSe, and Si$_2$OTe, respectively. We present the structural parameters of Si$_2$OX in Table 1.

To demonstrate the stability under normal conditions of Si$_2$OX materials, we examine their phonon dispersions. Fig. 2 presents the phonon spectra of three Si$_2$OX monolayers in the first Brillouin zone. Since the unitcell of Si$_2$OX contains 8 atoms, there are 24 vibrational branches within their vibrational spectra. It can be found that there are three acoustic and 21
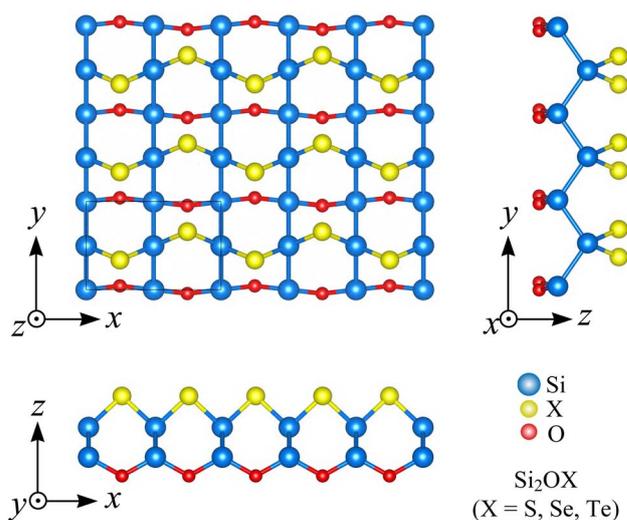

Fig. 1 Optimized crystal structures of Si$_2$OX monolayer in different views. The unitcell is denoted by the rectangle in the top view image.

Table 1 Optimized lattice constants a and b, chemical bond lengths d, bond angle ϕ, and elastic constants C_{ij} of Janus Si_2OX systems. Since the Janus Si_2OTe is unstable, the calculations for C_{ij} of Si_2OTe is excluded

	a (Å)	b (Å)	d_{Si-O} (Å)	d_{Si-X} (Å)	d_{Si-Si} (Å)	$\varphi_{\angle Si-O-Si}$ (°)	$\varphi_{\angle Si-X-Si}$ (°)	C_{11} (N m^{-1})	C_{12} (N m^{-1})	C_{22} (N m^{-1})	C_{66} (N m^{-1})
Si_2OS	5.92	3.90	1.71	2.13	2.36	120.29	87.82	92.34	−14.56	62.75	14.70
Si_2OSe	5.92	3.92	1.71	2.29	2.36	120.22	80.37	94.48	−5.79	69.99	18.00
Si_2SeTe	5.97	4.03	1.71	2.53	2.38	120.35	72.23	—	—	—	—
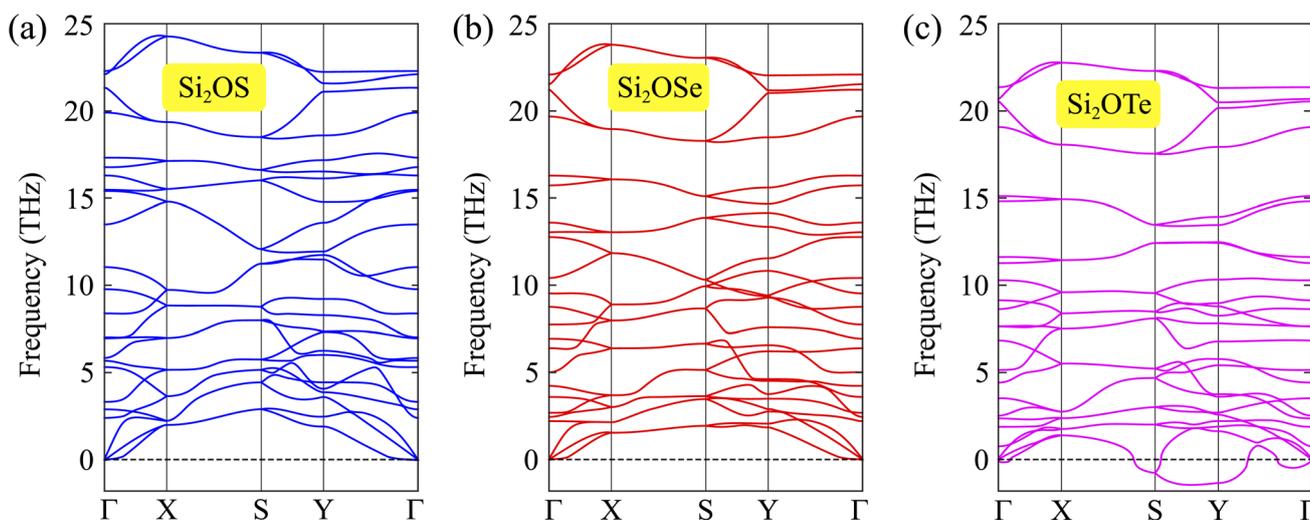
Fig. 2 Phonon dispersions along the Γ-X-S-Y-Γ high-symmetry line of Si_2OS (a), Si_2OSe (b), and Si_2OTe (c).

optical vibrational branches in the phonon dispersion. Besides, the frequencies of the vibrational branches of the two Janus Si_2OS and Si_2OSe are positive, while the negative frequencies are found in the vibrational spectrum of Si_2OTe as revealed in Fig. 2(c). Once the phonon dispersions contain the negative frequencies, the restoring forces against the displacement of the atoms are suppressed. As a consequence, the crystal structure of these materials is unstable. It implies that two monolayers Si_2OS and Si_2OSe are dynamically stable, while the Janus Si_2OTe monolayer is unstable. Therefore, from here on, we only examine Si_2OS and Si_2OSe and exclude Si_2OTe from the calculations due to its structural instability.

Next, the thermal stability of these two monolayers is also investigated through the AIMD simulation. We perform the AIMD test within 6 ps (each step of 1 fs) at room temperature (300 K). The total energy fluctuations of Si_2OS and Si_2OSe as functions of simulation time are illustrated in Fig. 3. It is obvious that the total energies fluctuate only by a very small value. The atomic structures of the two monolayers are only slightly deformed and remain structurally solid. Neither the structural phase transitions nor the breaking of chemical bonds were found after the AIMD simulation. It suggests that both Si_2OS and Si_2OSe are thermodynamic stable at ambient temperature.

Further, we also evaluate the mechanical stabilities of Janus Si_2OS and Si_2OSe monolayers based on the analysis their elastic characteristics. We calculate the elastic constants of 2D materials, namely C_{11}, C_{12}, C_{22}, and C_{66}, by using Duerloo's

method.[46] Two in-plane directions of the Janus systems are subjected to small uniaxial strains from −1.5% to 1.5%. At the specified strain, the positions of atoms are re-optimized and the
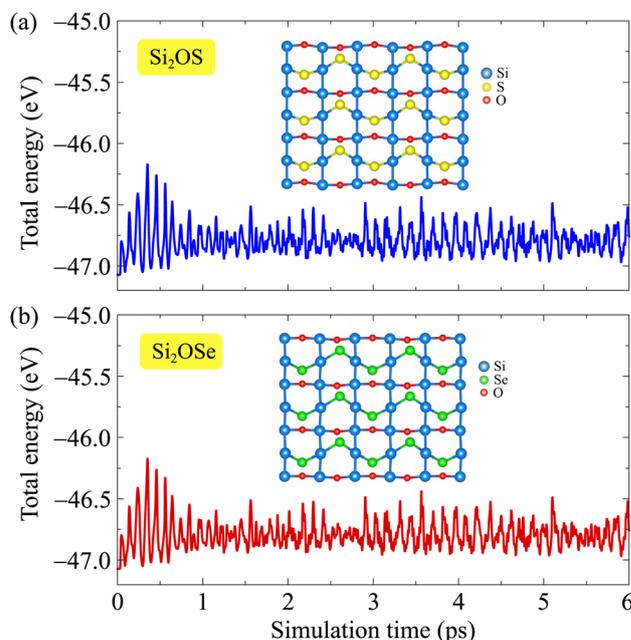
Fig. 3 AIMD calculations of Si_2OS (a) and Si_2OSe (b) systems. Inset presents the crystal structure at the end of the simulation progress.

strain-dependence of the energy is found. The calculated energies are polynomial fitted, which yields the in-plane stiffness coefficients. The in-plane stiffness coefficients of 2D Janus Si_2OS are found to be $C_{11} = 92.34$ N m^{-1} and $C_{22} = 62.75$ N m^{-1}, which are close to those of Si_2OSe being $C_{11} = 94.48$ N m^{-1} and $C_{22} = 69.99$ N m^{-1}, respectively. Particularly, both Si_2OS and Si_2OSe monolayers possess a negative value for elastic constant C_{12} ($C_{12} = -14.56$ N m^{-1} for Si_2OS and $C_{12} = -5.79$ N m^{-1} for Si_2OSe), suggesting that unusual NPR may occur in these investigated monolayers.[47,48] From the obtained elastic constants as listed in Table 1, it is revealed that C_{ij} of both Si_2OS and Si_2OSe monolayers satisfy the criteria proposed by Born for mechanical stabilities for 2D materials.[48,49] This indicates that the mechanical stability of Si_2OS and Si_2OSe is confirmed.

Next, we investigate the mechanical characteristics of Si_2OS and Si_2OSe through the calculations for Young's modulus and Poisson's ratio. The angular-dependent Young's modulus $Y_{2D}(\theta)$ and Poisson's ratio $\mathscr{P}(\theta)$ of the studied materials can be written by the following expressions:[50,51]

$$Y_{2D}(\theta) = \frac{C_{11}C_{22} - C_{12}{}^2}{C_{11} \sin^4 \theta - \Omega \sin^2 \theta \cos^2 \theta + C_{22} \cos^4 \theta}, \quad (1)$$

$$\mathscr{P}(\theta) = \frac{C_{12}(\sin^4 \theta + \cos^4 \theta) - \Pi \sin^2 \theta \cos^2 \theta}{C_{11} \sin^4 \theta - \Omega \sin^2 \theta \cos^2 \theta + C_{22} \cos^4 \theta}, \quad (2)$$

where $\Omega = 2C_{12} - (C_{11}C_{22} - C_{12}{}^2)/C_{66}$, $\Pi = C_{11} + C_{22} - (C_{11}C_{22} - C_{12}{}^2)/C_{66}$, and θ is the angle between the studied direction and the x-axis.

The angular-dependence of Young's modulus of the studied structures is depicted as shown in Fig. 4(a). Our calculated results revealed that Y_{2D} of Si_2OS and Si_2OSe monolayers are greatly directionally anisotropic. This is attributed to the in-plane asymmetric geometric structure of the Janus Si_2OX systems. The Si_2OSe monolayer has a larger Young's modulus value than that of Si_2OS monolayer. Young's modulus has the maximum value of 94.00 N m^{-1} (88.94 N m^{-1}) at $\theta = 0°$, and the minimum value of 48.35 N m^{-1} (39.28 N m^{-1}) at $\theta = 48°$ for the Janus Si_2OSe (Si_2OS) compound, respectively. Possessing a small Y_{2D}, Si_2OS and Si_2OSe monolayers have high mechanical flexibility compared to other 2D structures, such as graphene (344 N m^{-1}),[52] binary MoS_2 compound (130 N m^{-1})[53] or Janus ternary MoSSe monolayer (113 N m^{-1}).[54]

In Fig. 4(b), we reveal the calculated polar diagrams of Poisson's ratio P(θ) of Janus Si_2OS and Si_2OSe monolayers. It is found that Si_2OS and Si_2OSe monolayers exhibit a high anisotropy. Remarkably, the negative Poisson's ratio is found in both Si_2OS and Si_2OSe compounds. This is consistent with the expectation above that these structures have a negative C_{12}. The NPR feature can be seen in both x and y axes as depicted in Fig. 4(b). The calculated results demonstrate that Janus Si_2OS has a large in-plane NPR, up to -0.234 and -0.158 in the x and y axes, respectively. Surprisingly, these NPR values are much larger than those of SiS (-0.19 and -0.10)[48] and Janus Si_2SSe (-0.131 and -0.122 in the x and y axes, respectively).[35] The NPR values of Si_2OSe monolayer are found to be -0.083 (-0.061) in the x(y) axis as presented in Fig. 4(b). The appearance of the NPR confirms that Janus Si_2OS and Si_2OSe can be treated as auxetic semiconductors. Compared with usual nanomaterials, 2D auxetic structures possess many extraordinary physical features with promising application in various fields of nanotechnology.[55]

3.2 Electronic properties

Here, we report the electronic properties of two stable structures of Si_2OX, namely Si_2OS and Si_2OSe monolayers. First, the band structures of the two compounds are examined by both the PBE and HSE06 methods as shown in Fig. 5. It can be observed that Si_2OS and Si_2OSe monolayers exhibit indirect semiconducting characteristics. In the case of Si_2OS, the conduction band minimum (CBM) and valence band maximum (VBM) are found at the Γ point and on the $X\Gamma$ line, respectively. Meanwhile, the CBM and VBM of Si_2OSe are found respectively at the Y and Γ points. It should be noted that the vertical symmetric SiS and SiSe are direct bandgap semiconductors.[22,23] Thus, the symmetry breaking significantly changes the electronic characteristics of Janus structures. At the PBE level, the indirect bandgaps of Si_2OS and Si_2OSe monolayers are respectively obtained to be 1.35 and 1.20 eV. The bandgap correction by using the HSE06 functional shows that the bandgaps of Si_2OS and Si_2OSe monolayers are 2.18 and 1.97 eV, respectively. The obtained HSE06 bandgaps of Si_2OS and Si_2OSe are wider than those of SiS (1.22 eV)[23,56] and SiSe (1.44 eV[23] and 1.35 eV[56]). The obtained bandgaps of Si_2OS and Si_2OSe monolayers are listed in Table 2.
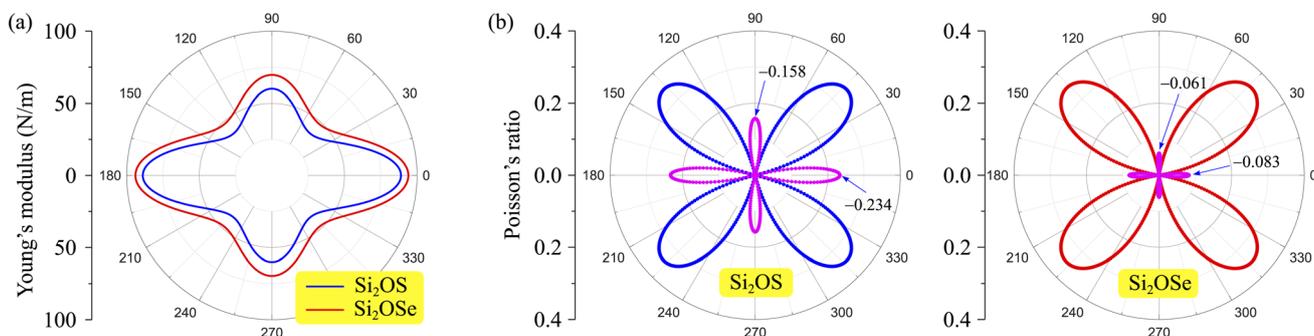
Fig. 4 (a) Young's modulus $Y_{2D}(\theta)$ and (b) Poisson's ratio P(θ) of Janus Si_2OS and Si_2OSe structures. Pink symbols in (b) indicate the negative values of P.
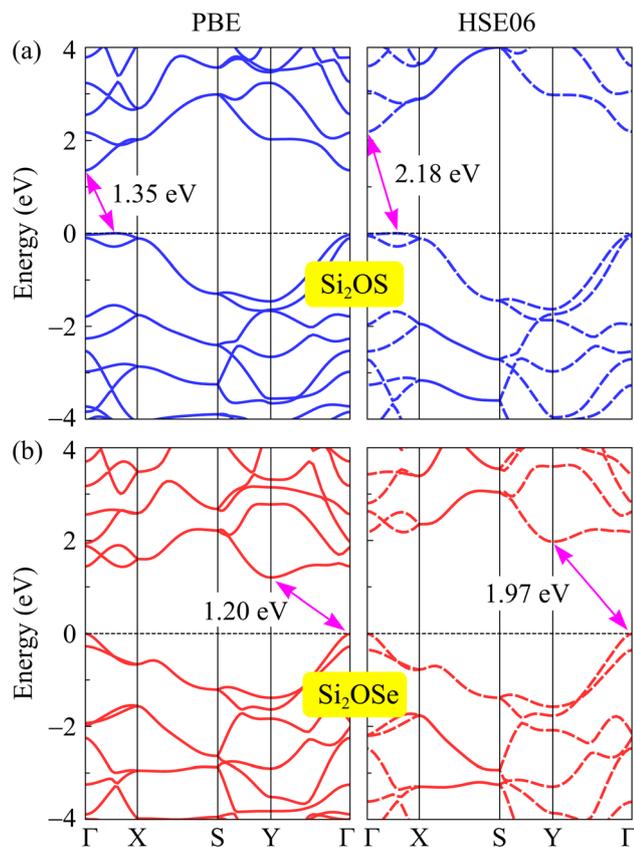
Fig. 5 The PBE and HSE06 band structures of Si$_2$OS (a) and Si$_2$OSe (b) monolayers.

Fig. 6 Electrostatic potentials of Si$_2$OS (a) and Si$_2$OSe (b) monolayers.

In addition to the electronic band diagrams, the work function is also a fundamental electronic feature of the material that should be taken into account. The work function denotes the required energy for electrons to escape from the surfaces of the studied structures and can be estimated based on the vacuum level E_{vac} and Fermi level E_F as: $\Phi = E_{vac} - E_F$. We can find the vacuum level based on calculations for the electrostatic potential of the studied structures. An intrinsic electric field exists in the vertical direction of the Janus material due to the electronegativity difference between the two sides of this layered structure. This difference in electronegativity leads to the vacuum level difference between the two sides of materials. As a consequence, there is a work function difference on the two sides of the studied asymmetric structures. Since the electronegativity of O atom is greater than that of the chalcogen atom X, the intrinsic electric field in the Si$_2$OX structures is directed from X to O. In Fig. 6, we show the electrostatic potential

energies with a dipole correction of Si$_2$OS and Si$_2$OSe materials. A vacuum level difference $\Delta\Phi$ is found in both Si$_2$OS and Si$_2$OSe. The larger the difference in atomic size between O and X elements, the larger the value $\Delta\Phi$ is. The calculated $\Delta\Phi$ for Si$_2$OS and Si$_2$OSe are 0.06 and 0.47 eV, respectively. Table 2 summarizes our obtained results for $\Delta\Phi$ and work functions of Si$_2$OS and Si$_2$OSe materials. The work functions of Si$_2$OS are slightly higher than those of Si$_2$OSe. The data in Table 2 reveal that it is easier for electrons to totally escape from the X surface than from the of O surface.

It is well-known that there are many techniques to tune the electronic features of 2D materials, such as chemical functionalization, defect effects, doping, etc. Among these, mechanical strain is an effective and simple approach to control electronic properties.[27,31,48] In this paper, a biaxial strain between −6% and 6% is applied to examine the strain-dependence of the electronic features of Si$_2$OS and Si$_2$OSe monolayers. The biaxial strain can be evaluated as $\varepsilon_b = (a - a_0)/a_0$, where a_0 and a denote the lattice constants of Si$_2$OS and Si$_2$OSe at equilibrium and strained states. Mechanical strains with positive and negative values correspond to tension and compression, respectively. Fig. 7 depicts the band structures of Si$_2$OS and Si$_2$OSe monolayers at several values of ε_b. We can see that the mechanical strain significantly adjusts the electronic band structures, especially for the Janus Si$_2$OS monolayer. When the tensile strain reaches +4%, the indirect–direct

Table 2 Obtained bandgaps E_g using PBE/HSE06 functional, difference between the vacuum levels $\Delta\Phi$, and work function on the O(X) side $\Phi_O(\Phi_X)$ of Si$_2$OX materials

	E_g^{PBE} (eV)	E_g^{HSE06} (eV)	$\Delta\Phi$ (eV)	Φ_O (eV)	Φ_X (eV)
Si$_2$OS	1.35	2.18	0.06	5.46	5.40
Si$_2$OSe	1.20	1.97	0.47	5.22	4.75

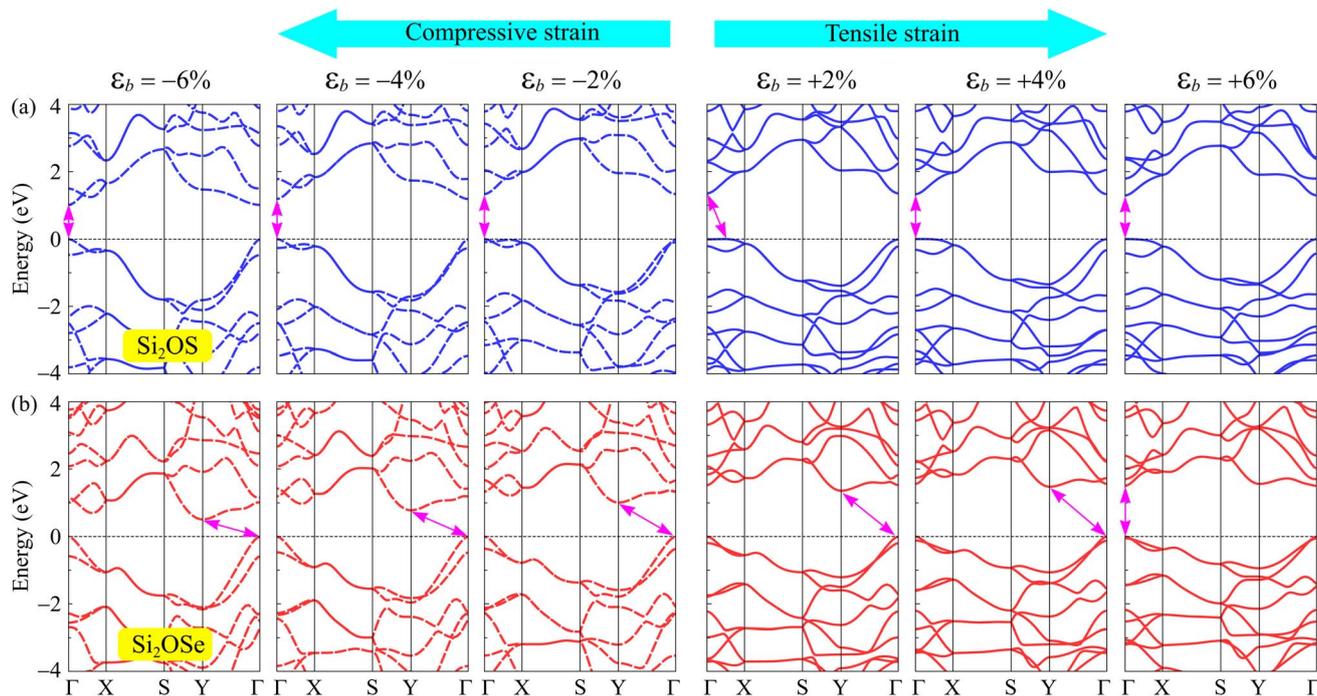**Fig. 7** The PBE band structures of (a) Si$_2$OS and (b) Si$_2$OSe materials under the biaxial strain ε_b.

bandgap transition is found in the Si$_2$OS structure as shown in Fig. 7(a). Also, Si$_2$OS is found as direct semiconductor with both VBM and CBM at the Γ point when the tensile strain is introduced. Both tensile and compressive strains shift the band edges in the electronic structure of the Janus structure, leading to a change in the bandgap. Besides, the phase transition from indirect to direct bandgap is also observed in Si$_2$OSe monolayer at $\varepsilon_b = 6\%$ and the applied strain significantly modulates its bandgap. Fig. 8 presents the bandgaps of Janus Si$_2$OX structures as functions of ε_b. As can be seen from Fig. 8, the bandgap of Si$_2$OSe is significantly reduced by compressive strains, whereas tensile strain slightly increases its bandgap. In the case of Si$_2$OS,

the biaxial strains reduce its bandgap. However, the effect of ε_b on the energy gap of Si$_2$OS is quite weak. The maximum bandgap of Si$_2$OS is 1.35 eV at equilibrium ($\varepsilon_b = 0$) and the lowest is at $\varepsilon_b = -6$ with the value of 1.01 eV. The strain-induced phase transitions from indirect-to-direct energy gap in both Si$_2$OS and Si$_2$OS make them promising for nanoelectromechanical applications.

3.3 Carrier mobility

In the following, we compute the carrier mobilities in Janus Si$_2$OS and Si$_2$OXSe materials. Carrier mobility is a key parameter relevant to technological applications such as electronic devices. By employing the deformation potential (DP) approximation,[45] the mobilities of electrons and holes in 2D systems can be obtained by the following equation:[57]

$$\mu_{2D} = \frac{e\hbar^3 C_{2D}}{k_B T m^* \overline{m} E_d^2},$$ (3)

where e, $\hbar$, k_B, and T refer to the elementary charge, the reduced Planck's constant, Boltzmann's constant, and the temperature, respectively. m^* and $\overline{m} = \sqrt{m_x^* m_y^*}$ are respectively the carrier effective mass along the x/y axis and average effective mass. C_{2D} refers to the elastic modulus and E_d indicates the DP constant. Herein, the carrier mobility is calculated at $T = 300$ K (room temperature). The effective mass of carriers, elastic modulus, and the DP constant are determined as follows:

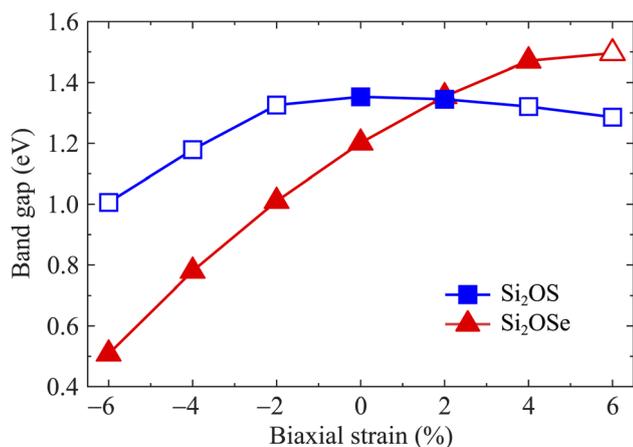$$\frac{1}{m^*} = \frac{1}{\hbar^2} \left| \frac{\partial^2 E(k)}{\partial k^2} \right|,$$ (4)

Fig. 8 Dependence of the bandgaps of Si$_2$OS and Si$_2$OSe on the biaxial strain ε_b. The filled/empty shapes indicate the indirect/direct bandgaps, respectively.
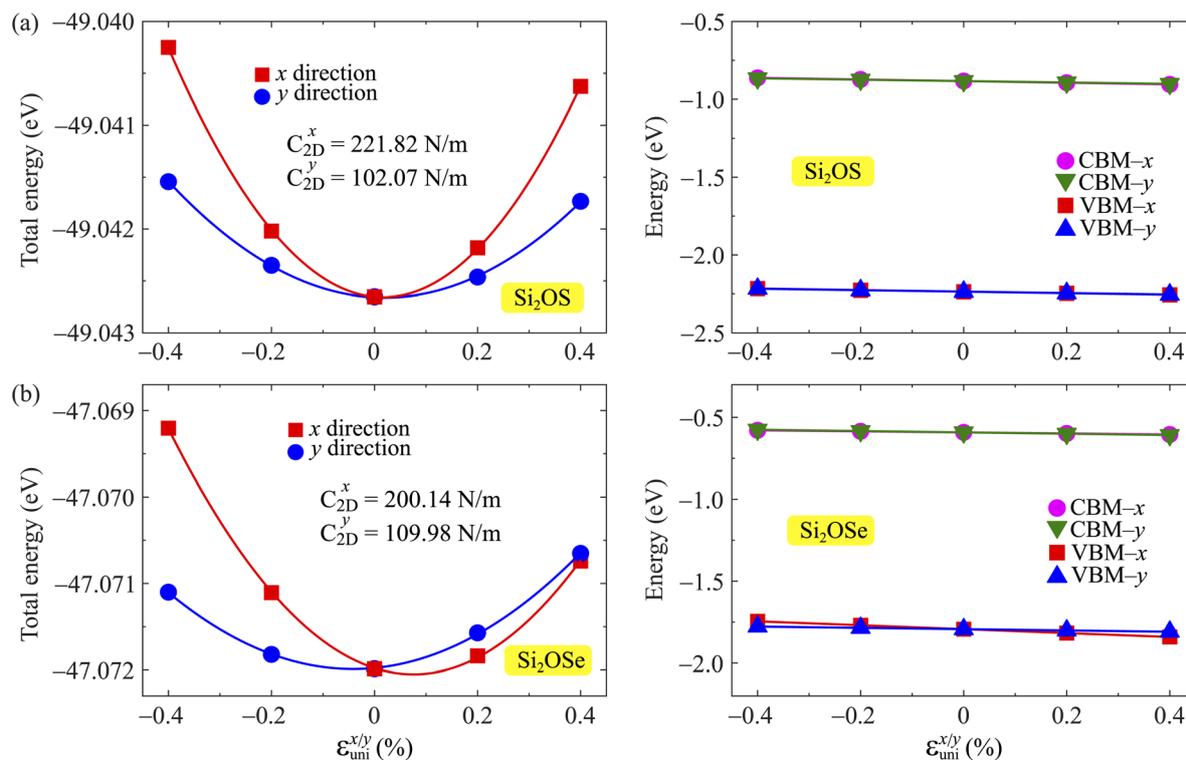
Fig. 9 The total energy and band-edge energy of Si_2OS (a) and Si_2OSe (b) monolayers as functions of small uniaxial strains $\varepsilon_{uni}^{x/y}$.

$$C_{2D} = \frac{1}{V_0} \frac{\partial^2 E_{tot}}{\partial \varepsilon_{uni}^2}, \tag{5}$$

$$E_d = \frac{\Delta E_{edge}}{\varepsilon_{uni}}, \tag{6}$$

where $E(k)$ indicates the wavenumber k-dependent energy at the VBM for holes and CBM for electrons. V_0 and E_{tot} refer to the area of optimized unitcell and the total energy, respectively. ε_{uni} is the small uniaxial strain along the x/y axis, which varies between 0 and $\pm 0.4\%$ in our calculations for the transport parameters. ΔE_{edge} stands for the uniaxial strain-induced energy change of the band edges. The transport parameters C_{2D} and E_d are obtained by fitting the strain-dependence of the total energies and band edges energy as presented in Fig. 9. The total energy depends not only strongly on the strain but also on the direction of the uniaxial strain, namely along the x or y axis. This will cause the elastic modulus of the examined structures to be high and they are high directional anisotropy. Meanwhile, the change in position of the band edges of Si_2OS and Si_2OSe

monolayers in the presence of the applied uniaxial strains along the x and y axes is small, suggesting that the directional isotropy of the DP constant is high.

The obtained transport parameters m^*, C_{2D}, E_d, and corresponding carrier mobility μ_{2D} along the axes x and y are presented in Table 3. We can see that Janus Si_2OS and Si_2OXSe exhibit highly directionally anisotropic transport features due their in-plane anisotropic crystal lattice. The results of our calculations indicate that the electrons in Janus Si_2OS and Si_2OXSe monolayers have low effective mass. The electron effective masses of Si_2OS and Si_2OXSe along the $x(y)$ directions are respectively $0.48m_0$ $(0.50m_0)$ and $0.59m_0$ $(1.39m_0)$ with m_0 being the free electron mass. Since the electrons have a low effective mass, they will respond quickly to the external field, which is expected to result in high electron mobilities in the Janus Si_2OS and Si_2OXSe monolayers. In Janus Si_2OS, the electrons have a smaller effective mass than that of the holes. Meanwhile, the hole effective masses of Si_2OSe are smaller than those of the electrons. These results are consistent with the band dispersion

Table 3 The calculated effective masses of carriers m^* (in unit of the mass of a free electron m_0), elastic modulus C_{2D} (N m^{-1}), DP constant E_d (eV), and carrier mobility μ_{2D} (cm^2 V^{-1} s^{-1}) along the x/y transport axis of Si_2OS and Si_2OSe monolayers

		m_x^*	m_x^*	C_{2D}^x	C_{2D}^y	E_d^x	E_d^y	μ_{2D}^x	μ_{2D}^y
Si_2OS	Electron	0.48	0.50	221.82	102.07	−5.25	−4.47	727.98	443.60
	Hole	1.57	6.21	221.82	102.07	−4.96	−4.65	39.12	5.17
Si_2OSe	Electron	0.59	1.39	200.14	109.98	−3.21	−4.10	773.26	110.56
	Hole	0.4	0.38	200.14	109.98	−11.95	−3.96	191.16	1.01×10^3

as shown in Fig. 5. For example, the band structure of Si_2OSe around the VBM is flatter than that around the CBM as presented in Fig. 5(a). The flatter the band structure at the band edge (the larger the curvature radius), the smaller the second derivative $\partial^2 E(k)/\partial k$,^{2} leading to a large effective mass.

Table 3 reveals that electron mobility and hole mobility are both directionally anisotropic. The electron mobility μ_{2D} along the x axis is much higher than that along the y axis for both studied Janus structures. The electron mobilities of Si_2OS are calculated to be $\mu_{2D}^y = 727.98$ cm^2 V^{-1} s^{-1} and $\mu_{2D}^x = 443.60$ cm^2 V^{-1} s^{-1}, which are high enough for applications in nanoelectronic devices.[58] The electron mobilities of Si_2OS monolayer are comparable with obtained results for Janus Si_2SSe $\mu_{2D}^y = 897.66$ cm^2 V^{-1} s^{-1} and $\mu_{2D}^x = 627.13$ cm^2 V^{-1} s^{-1}.[35] The anisotropy in electron mobility is evident in the Si_2OSe monolayer, where the electron mobility along x direction μ_{2D}^x is about 7 times higher than μ_{2D}^y. The calculated results for carrier mobility of Janus Si_2OS and Si_2OXSe monolayers are listed in Table 3. It should also be mentioned that the holes in Si_2OXSe have high mobility, up to 1000 cm^2 V^{-1} s^{-1} along the y axis, which is greater than the electron mobility.

4 Conclusions

Based on DFT calculations, we have reported the structural, mechanical, electronic, and transport features of 2D Janus structures Si_2OX (X = S, Se, Te). Our results demonstrated that the Si_2OS and Si_2OSe monolayers are highly stable structures while Si_2OTe monolayer is an unstable structure with large negative frequencies in its phonon spectrum. The auxetic effect has been found in the two investigated stable monolayers with large NPR values. Especially, the Si_2OS structure possesses a very high NPR, up to -0.234 in the x-axis. The studied monolayers Si_2OS and Si_2OSe are both indirect band gap semiconductors and the transitions from indirect to direct band gap have been found in these structures when the biaxial strains are introduced. In addition, carrier mobility in both considered Janus structures is very high and anisotropic. Our findings reveal the novel properties of Janus Si_2OX structures and great potential in multifunctional applications.

Conflicts of interest

There are no conflicts to declare.

Acknowledgements

References

1 C. W. Huang, W. Ren, V. C. Nguyen, Z. Chen, J. Wang, T. Sritharan and L. Chen, *Adv. Mater.*, 2012, **24**, 4170–4174.

2 R. Lakes, *Science*, 1987, **235**, 1038–1040.

3 X. Xu, Q. Zhang, M. Hao, Y. Hu, Z. Lin, L. Peng, T. Wang, X. Ren, C. Wang, Z. Zhao, C. Wan, H. Fei, L. Wang, J. Zhu, H. Sun, W. Chen, T. Du, B. Deng, G. J. Cheng, I. Shakir, C. Dames, T. S. Fisher, X. Zhang, H. Li, Y. Huang and X. Duan, *Science*, 2019, **363**, 723–727.

4 F. Milstein and K. Huang, *Phys. Rev. B: Condens. Matter Mater. Phys.*, 1979, **19**, 2030–2033.

5 J. F. Silveira and A. R. Muniz, *Carbon*, 2017, **113**, 260–265.

6 B. Saha and A. Datta, *J. Phys. Chem. C*, 2018, **122**, 19204–19211.

7 B. Saha, S. M. Pratik and A. Datta, *Chem.–Eur. J.*, 2017, **23**, 12917–12923.

8 J.-W. Jiang and H. S. Park, *Nat. Commun.*, 2014, **5**, 4727.

9 A. J. Mannix, X.-F. Zhou, B. Kiraly, J. D. Wood, D. Alducin, B. D. Myers, X. Liu, B. L. Fisher, U. Santiago, J. R. Guest, M. J. Yacaman, A. Ponce, A. R. Oganov, M. C. Hersam and N. P. Guisinger, *Science*, 2015, **350**, 1513–1516.

10 Y. Wang, F. Li, Y. Li and Z. Chen, *Nat. Commun.*, 2016, **7**, 11488.

11 S. Woo, H. C. Park and Y.-W. Son, *Phys. Rev. B*, 2016, **93**, 075420.

12 L. Yu, Q. Yan and A. Ruzsinszky, *Nat. Commun.*, 2017, **8**, 15224.

13 X. Li, X. Qiang, Z. Gong, Y. Zhang, P. Gong and L. Chen, *Research*, 2021, **2021**, 1904839.

14 A. Alderson and K. L. Alderson, *Proc. Inst. Mech. Eng.*, 2007, **221**, 565–575.

15 W. Yang, Z.-M. Li, W. Shi, B.-H. Xie and M.-B. Yang, *J. Mater. Sci.*, 2004, **39**, 3269–3279.

16 C. Huang and L. Chen, *Adv. Mater.*, 2016, **28**, 8079–8096.

17 F. Scarpa, *IEEE Signal Process. Mag.*, 2008, **25**, 126–128.

18 M. Avellaneda and P. J. Swart, *J. Acoust. Soc. Am.*, 1998, **103**, 1449–1467.

19 T. C. Phong and L. T. T. Phuong, *Phys. B*, 2023, **666**, 415119.

20 T. C. Phong, V. T. T. Vi and L. T. T. Phuong, *Phys. Lett. A*, 2023, **480**, 128946.

21 T. C. Phong, N. T. Nam and L. T. T. Phuong, *Phys. Lett. A*, 2023, **474**, 128830.

22 J.-H. Yang, Y. Zhang, W.-J. Yin, X. G. Gong, B. I. Yakobson and S.-H. Wei, *Nano Lett.*, 2016, **16**, 1110–1117.

23 T. Jing, D. Liang, M. Deng and S. Cai, *J. Mater. Chem. C*, 2020, **8**, 10382–10389.

24 A.-Y. Lu, H. Zhu, J. Xiao, C.-P. Chuu, Y. Han, M.-H. Chiu, C.-C. Cheng, C.-W. Yang, K.-H. Wei, Y. Yang, Y. Wang, D. Sokaras, D. Nordlund, P. Yang, D. A. Muller, M.-Y. Chou, X. Zhang and L.-J. Li, *Nat. Nanotechnol.*, 2017, **12**, 744.

25 J. Zhang, S. Jia, I. Kholmanov, L. Dong, D. Er, W. Chen, H. Guo, Z. Jin, V. B. Shenoy, L. Shi and J. Lou, *ACS Nano*, 2017, **11**, 8192–8198.

26 T. V. Vu, V. T. T. Vi, H. V. Phuc, A. I. Kartamyshev and N. N. Hieu, *Phys. Rev. B*, 2021, **104**, 115410.

27 T. V. Vu, C. V. Nguyen, H. V. Phuc, A. A. Lavrentyev, O. Y. Khyzhun, N. V. Hieu, M. M. Obeid, D. P. Rai, H. D. Tong and N. N. Hieu, *Phys. Rev. B*, 2021, **103**, 085422.

28 N. N. Hieu, H. V. Phuc, A. I. Kartamyshev and T. V. Vu, *Phys. Rev. B*, 2022, **105**, 075402.

29 T. V. Vu, H. V. Phuc, A. I. Kartamyshev and N. N. Hieu, *Appl. Phys. Lett.*, 2023, **122**, 061601.

30 T. V. Vu, V. T. T. Vi, C. V. Nguyen, H. V. Phuc and N. N. Hieu, *J. Phys. D: Appl. Phys.*, 2020, **53**, 455302.

31 T. V. Vu, V. T. T. Vi, H. V. Phuc, C. V. Nguyen, N. A. Poklonski, C. A. Duque, D. P. Rai, B. D. Hoi and N. N. Hieu, *J. Phys.: Condens.Matter*, 2021, **33**, 225503.

32 L. Dong, J. Lou and V. B. Shenoy, *ACS Nano*, 2017, **11**, 8242–8248.

33 A. Mogulkoc, Y. Mogulkoc, S. Jahangirov and E. Durgun, *J. Phys. Chem. C*, 2019, **123**, 29922–29931.

34 X. Yan, X. Cui, B. Wang, H. Yan, Y. Cai and Q. Ke, *Iscience*, 2023, **26**, 106731.

35 N. T. Hiep, C. Q. Nguyen and N. N. Hieu, *Appl. Phys. Lett.*, 2023, **123**, 092102.

36 G. Kresse and J. Furthmüller, *Phys. Rev. B: Condens. Matter Mater. Phys.*, 1996, **54**, 11169–11186.

37 G. Kresse and J. Furthmüller, *Comput. Mater. Sci.*, 1996, **6**, 15–50.

38 J. P. Perdew, K. Burke and M. Ernzerhof, *Phys. Rev. Lett.*, 1996, **77**, 3865.

39 J. Neugebauer and M. Scheffler, *Phys. Rev. B: Condens. Matter Mater. Phys.*, 1992, **46**, 16067–16080.

40 H. J. Monkhorst and J. D. Pack, *Phys. Rev. B: Solid State*, 1976, **13**, 5188–5192.

41 J. Heyd, G. E. Scuseria and M. Ernzerhof, *J. Chem. Phys.*, 2003, **118**, 8207.

42 S. Grimme, J. Antony, S. Ehrlich and H. Krieg, *J. Chem. Phys.*, 2010, **132**, 154104.

43 A. Togo, L. Chaput and I. Tanaka, *Phys. Rev. B: Condens. Matter Mater. Phys.*, 2015, **91**, 094306.

44 S. Nosé, *J. Chem. Phys.*, 1984, **81**, 511.

45 J. Bardeen and W. Shockley, *Phys. Rev.*, 1950, **80**, 72.

46 K.-A. N. Duerloo, M. T. Ong and E. J. Reed, *J. Phys. Chem. Lett.*, 2012, **3**, 2871–2876.

47 X. Zhou, N. Zhou, C. Li, H. Song, Q. Zhang, X. Hu, L. Gan, H. Li, J. Lü, J. Luo, J. Xiong and T. Zhai, *2D Mater.*, 2017, **4**, 025048.

48 T. Jing, D. Liang, M. Deng and S. Cai, *J. Mater. Chem. C*, 2020, **8**, 10382–10389.

49 M. Born and K. Huang, *Am. J. Phys.*, 1955, **23**, 474.

50 N. T. Hung, A. R. T. Nugraha and R. Saito, *J. Phys. D: Appl. Phys.*, 2018, **51**, 075306.

51 P. Xiang, S. Sharma, Z. M. Wang, J. Wu and U. Schwingenschlögl, *ACS Appl. Mater. Interfaces*, 2020, **12**, 30731.

52 E. Cadelano, P. L. Palla, S. Giordano and L. Colombo, *Phys. Rev. B: Condens. Matter Mater. Phys.*, 2010, **82**, 235414.

53 R. C. Cooper, C. Lee, C. A. Marianetti, X. Wei, J. Hone and J. W. Kysar, *Phys. Rev. B: Condens. Matter Mater. Phys.*, 2013, **87**, 035423.

54 S.-D. Guo, *Phys. Chem. Chem. Phys.*, 2018, **20**, 7236–7242.

55 R. Peng, Y. Ma, Z. He, B. Huang, L. Kou and Y. Dai, *Nano Lett.*, 2019, **19**, 1227–1233.

56 J.-H. Yang, Q. Yuan, H. Deng, S.-H. Wei and B. I. Yakobson, *J. Phys. Chem. C*, 2017, **121**, 123–128.

57 W. Wan, S. Zhao, Y. Ge and Y. Liu, *J. Phys.: Condens.Matter*, 2019, **31**, 435501.

58 B. Radisavljevic, A. Radenovic, J. Brivio, V. Giacometti and A. Kis, *Nat. Nanotechnol.*, 2011, **6**, 147–150.